

1 The optimum fire window: applying the fire-productivity  
2 hypothesis to Jurassic climate states

3  
4  
5 Teuntje P. Hollaar\*<sup>1,2</sup>, Claire M. Belcher<sup>1</sup>, Micha Ruhl<sup>3</sup>, Jean-François Deconinck<sup>4</sup>, Stephen P.  
6 Hesselbo<sup>2,5</sup>  
7

8 <sup>1</sup>WildFIRE Lab, Global Systems Institute, University of Exeter, Exeter, EX4 4PS, UK

9 <sup>2</sup>Camborne School of Mines, Department of Earth and Environmental Sciences, University of Exeter,  
10 Penryn Campus, Penryn, TR10 9FE, UK

11 <sup>3</sup>Department of Geology, Trinity College Dublin, The University of Dublin, College Green, Dublin,  
12 Ireland

13 <sup>4</sup>Biogéosciences, UMR 6282 CNRS, Université de Bourgogne/Franche-Comté, 21000 Dijon, France

14 <sup>5</sup>Environment and Sustainability Institute, University of Exeter, Penryn Campus, Penryn, TR10 9FE,  
15 UK

16 \*Corresponding author: t.p.hollaar@uu.nl  
17

18 **Abstract**

19 Present day fire frequency has been related to a productivity/aridity gradient on a regional and global  
20 scale. Optimum fire conditions occur at times of intermediate productivity and aridity, whereas fire is  
21 limited on the high productivity (moisture) and aridity (no fuel) endmembers. However, the current  
22 global fire activity pattern is reinforced by the predominant burning of grasslands. Here we test the  
23 intermediate fire-productivity hypothesis for a period on Earth before the evolution of grasses, the  
24 Early Jurassic, and explore the fire regime of two contrasting climatic states: the Late Pliensbachian  
25 (LPE) cooling Event and the Sinemurian–Pliensbachian Boundary (SPB) warming. Palaeo-fire  
26 records are reconstructed from fossil charcoal abundance, and changes in the hydrological cycle are  
27 tracked via clay mineralogy, which allows inference of changes in fuel moisture status. Large  
28 fluctuations in the fossil charcoal on an eccentricity time scale indicate two modes of fire regime at  
29 the time. Wildfires were moisture limited in a high productivity ecosystem during eccentricity minima  
30 for both the SPB and LPE. During eccentricity maxima, fires increased, and an optimum fire window  
31 was reached, in which greater seasonality in rainfall and temperatures led to intermediate states of  
32 productivity and aridity. The LPE experienced more extreme climatic endmembers compared to the  
33 SPB, with the fire regime edging closer to ‘moisture limitation’ during eccentricity minima, and more

34 pronounced seasonality during eccentricity maxima, explained by the overall cooler climate at the  
35 time. This study illustrates that the intermediate-productivity gradient holds up during two contrasting  
36 climatic states in the Jurassic.

37

### 38 **Plain Language Summary**

39 Fires are limited in year-round wet climates (tropical rainforests, too wet), and in year-round dry  
40 climates (deserts, no fuel). This concept, the intermediate-productivity gradient, explains the global  
41 pattern of fire activity. Here we test this concept for climate states of the Jurassic (~190 Myr ago). We  
42 find that the intermediate-productivity gradient also applies in the Jurassic, despite the very different  
43 ecosystem assemblages, with fires most frequent at times of high seasonality.

44

### 45 **Key Points**

- 46 • The intermediate-fire productivity gradient can be applied to the Jurassic and be utilized to  
47 explain changes in biomass abundance, moisture availability, and fire activity.
- 48 • The terrestrial ecosystem surrounding the Cardigan Bay Basin was not year-round dry during  
49 the Sinemurian–Pliensbachian Boundary warming Event or the Late Pliensbachian Cooling  
50 Event and therefore fire was not aridity limited.
- 51 • Fire activity was strongly influenced by the ~100 kyr and 405 kyr eccentricity cycle during  
52 both climatic states, which led to two modes in the fire regime: productivity limited (minima)  
53 and the optimum fire-window (maxima).

54

55

56

57

58

59

60

61

62

63 **1 Introduction**

64 The global distribution of fire at the present day follows the intermediate-productivity hypothesis.  
65 This hypothesis suggests that fire activity increases non-linearly along a productivity gradient  
66 primarily controlled by biomass and fuel availability (Pausas & Bradstock, 2007; Pausas & Ribeiro,  
67 2013). Climate drives fuel availability, structure, and moisture, which are the main determinants of the  
68 fire regime. Where the fire regime reflects the frequency, behaviour, type of fire, and the impact on  
69 the ecosystem (Bradstock, 2010). Fire is either limited by high moisture in ecosystems with high  
70 biomass production, for example in tropical rainforests, or in high aridity and low biomass production  
71 ecosystems, with disconnected fuel such as in deserts. This principle explains drought-driven fire  
72 regimes and fuel-limited fire regimes (Pausas & Ribeiro, 2013). In humid regions fires are initiated by  
73 seasonal aridity which leads to flammable conditions and lower fuel-moisture status. Rising  
74 temperatures can lead to increased drought and flammability in high productivity ecosystems and  
75 further accelerate this drought-driven increase in fire activity (Pausas & Ribeiro, 2013). In  
76 unproductive arid regions it is biomass production that determines fire activity, as the fuel-moisture  
77 status would not be limiting (Pausas & Ribeiro, 2013). The optimum window for wildfires is at  
78 intermediate productivity levels, such as in the tropical savannahs of today, wherein biomass can  
79 accumulate due to seasonal precipitation and fuel becomes available in the dry season when the fuel  
80 moisture status decreases (Meyn et al., 2007; Pausas & Bradstock, 2007; Krawchuk & Moritz, 2011;  
81 Pausas & Paula, 2012; Pausas & Ribeiro, 2013).

82  
83 The intermediate-productivity concept provides an effective explanation for the distribution of fire on  
84 a global and regional scale in the modern day where highest fire activity is found at intermediate  
85 moisture availability (Meyn et al., 2007; Krawchuk & Moritz, 2011; Daniau et al., 2012). The  
86 observation of high fire activity in ecosystems that are of intermediate aridity and productivity is  
87 strongly driven by grass biomes today (Archibald et al., 2018), where >80 % of area burnt is in  
88 grasslands (van der Werf et al., 2006). Although the intermediate-productivity gradient hypothesis of  
89 the present day is strongly linked to the expanse of grassland habitats, it should not require the  
90 presence of grasses to explain the impact of climate and seasonality on fire frequency in other  
91 vegetation types. The crucial concept is that an optimum fire window exists when there is a  
92 sufficiently moist season that allows fuel growth which is followed by a drier season in which fuel  
93 moisture levels are lowered, allowing ignition and fire spread. Since fire has formed an important part  
94 of ecosystems and the Earth system since 420 Ma (Glasspool et al., 2004; Glasspool & Gastaldo,  
95 2022), we therefore test whether the intermediate-productivity gradient has also existed and if the  
96 concept can also be applied in a world before the evolution of grasses.

97  
98 Here we look back at two contrasting climate events in the Early Jurassic, ~190 Myr ago, to assess  
99 what evidence there is for the existence of the intermediate-productivity fire gradient at such time

100 (Fig. 1). The first event, the Sinemurian-Pliensbachian Boundary event (SPB, is marked by global  
101 warming, sea-level rise, increased humidity, and a negative carbon-isotope excursion (Ruhl et al.,  
102 2016; Haq, 2018; Deconinck et al., 2019; Storm et al., 2020). In contrast, the second event, the late  
103 Pliensbachian Event (LPE) is marked by ~5 °C cooling in NW Europe, greater aridity, sea-level fall  
104 and a global positive carbon-isotope excursion (e.g. Korte et al., 2015; Ruhl et al., 2016; Haq, 2018;  
105 Deconinck et al., 2019; Storm et al., 2020). We couple charcoal, clay and climate data to infer palaeo-  
106 fire and the hydrological regimes during both these time intervals.

107

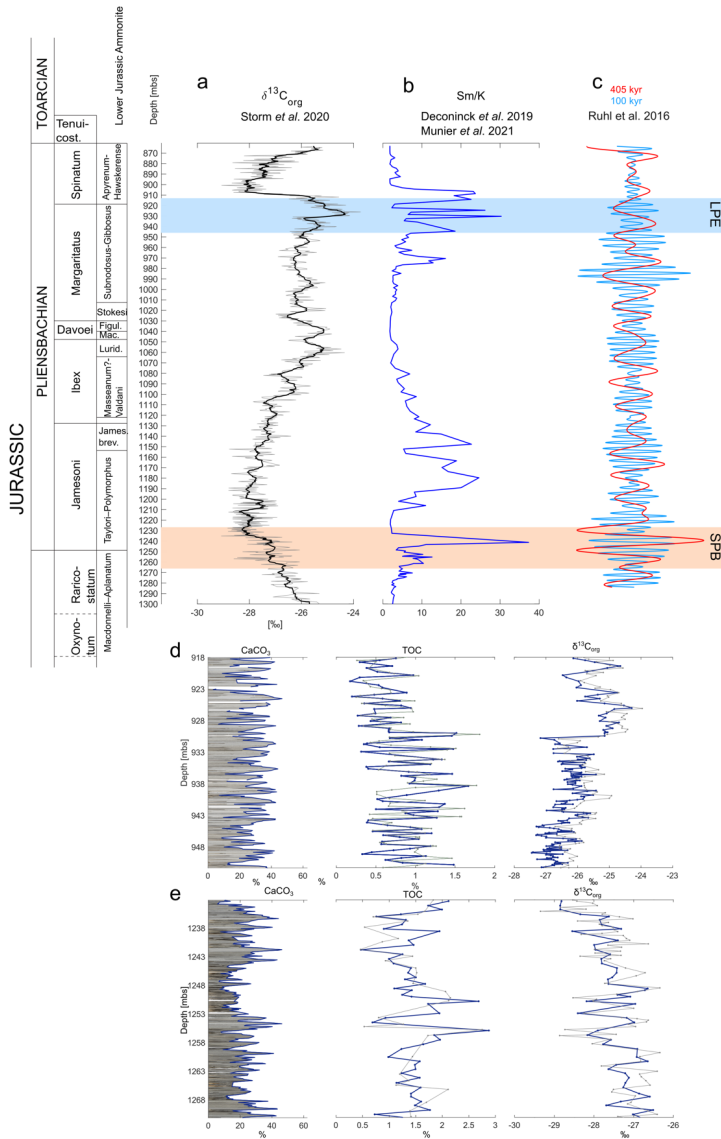
## 108 2 Materials and Methods

### 109 Materials

110 The records from both ~~the LPE and SPB~~ are taken from the Llanbedr (Mochras Farm) borehole, from  
111 sedimentary strata deposited in a relatively deep marine setting close to the shore in the Cardigan Bay  
112 Basin (Wales, UK). These sediments show a strong regular orbital control in the limestone-mudstone  
113 alternations (Ruhl et al., 2016), and an existing astrochronological framework provides an age model  
114 for the Mochras borehole. In addition, input of terrestrial organic matter in the sampled section is  
115 relatively high (van de Schootbrugge et al., 2005; Riding et al., 2013), and thus provides ideal  
116 material to study palaeo-fire regimes with a relatively high temporal constraint.

Deleted: time

Deleted: periods



119

120 **Fig. 1:** Cyclostratigraphic framework of the latest Sinemurian–Pliensbachian of the Mochras core  
 121 and the two intervals here studied. Red bar represents the interval (1271–1233 metres below surface  
 122 (mbs)) of the SPB and the blue bar represents the interval of the LPE (951–918 mbs) (a) The  $\delta^{13}\text{C}_{\text{org}}$   
 123 record from the Mochras core (Storm et al., 2020), shows the broad negative carbon-isotope trend  
 124 around the SPB and the positive carbon-isotope excursion (CIE) in the Late Pliensbachian. (b) The

125 smectite/kaolinite (Sm/K) ratio reflects changes in the hydrological cycle; data from Deconinck et al.  
126 (2019) and Munier et al. (2021). Peaks in smectite indicate greater climatic aridity (Deconinck et al.,  
127 2019; Munier et al., 2021). (c) ~~The bandpass-filtered Ca-elemental record in the depth domain from~~  
128 ~~Ruhl et al. (2016) representing the 100 kyr and 405 kyr cycle.~~ (d) The LPE interval is carbonate-rich  
129 and shows the metre-scale variations in CaCO<sub>3</sub> and TOC, next to the  $\delta^{13}C_{org}$  positive shifts that marks  
130 the onset of the LPE. (e) The SPB interval contains relatively more clay and lithological couplets of  
131 alternating CaCO<sub>3</sub> and TOC-enhanced beds occurring on a metre scale. The  $\delta^{13}C_{org}$  shows the  
132 negative trend of the long-negative limb of the SPB negative CIE.

Deleted: B

Deleted:

Deleted: s of the 100 kyr and 405 kyr cycle based on the Ca-elemental record in the depth domain from Ruhl et al. (2016).

Formatted: Font: Italic

133 The Mochras core was drilled between 1967 and 1969 on the coast in NW Wales, UK. Preserved 1-m-  
134 length core slabs of the core are stored at the British Geological Survey National Core Repository at  
135 Keyworth, United Kingdom. The Pliensbachian of Mochras shows alternating beds of pale grey  
136 limestone and dark brown to grey mudstone (Ruhl et al., 2016). These couplets occur throughout the  
137 Pliensbachian, but vary in thickness, from about 90 cm at the Sinemurian–Pliensbachian boundary to  
138 about 30 cm in the Late Pliensbachian age strata (latest Margaritatus and Spinatum zones) (Ruhl et al.,  
139 2016). The lithological couplets are well expressed around the SPB and in the Margaritatus Zone  
140 (Ruhl et al., 2016). For this study, samples were taken at an average sample spacing of 90 cm across  
141 the Sinemurian–Pliensbachian boundary (1272–1233 mbs (metres below surface)). In addition, data  
142 are utilized in this study that are published in Hollaar et al. (2021; 2023), from the Late Pliensbachian  
143 interval that is sampled at a 10 cm (951–934 mbs) and 30 cm (934–918 mbs) resolutions. The  
144 macrocharcoal data between 934–918 mbs are new and not previously published. An overview of the  
145 number of samples per stratigraphic interval and proxy can be found in SI Table 1.

#### 146 *Palaeolocation and provenance*

147 During the Early Jurassic, the Mochras site was situated in the Boreal realm of the Laurasian Seaway,  
148 which contained an island archipelago, and covers most of present-day NW and W Europe. The  
149 Mochras site was situated at a palaeolatitude of  $\sim 35^\circ$  N (Torsvik & Cocks, 2017), just off the Welsh  
150 Massif, in a relatively deep marine setting, below storm base (Pieńkowski et al., 2021), but with a  
151 strong terrestrial influence (van de Schootbrugge et al., 2005; Riding et al., 2013; Xu et al., 2018;  
152 Storm et al., 2020).

Deleted:

153 The Welsh Massif was likely the main detrital source to the Cardigan Bay Basin (Deconinck et al.,  
154 2019), although other emergent areas in proximity likely also contributed (Deconinck et al., 2019).  
155 The nearby Irish Massif, situated west of the Welsh Massif, also cannot be dismissed as a source of  
156 nutrients, terrestrial organic particles, clay and coarser mineral grains to the Cardigan Bay Basin  
157 (Deconinck et al., 2019). Another possible source area is the emergent land of the Scottish Massif to  
158 the north of the Mochras Borehole and the London-Brabant Massif to the east of the Mochras  
159 Borehole (van de Schootbrugge et al., 2005).

165 The multiple nearby landmasses contributing runoff to the here studied relatively deeper marine  
166 depositional environment, allowed for the charcoal record presented in this study to reflect a regional  
167 expression of likely multiple fires. These fires might have in part occurred synchronous, but it is also  
168 important to note that one stratigraphic rock sample in this study represents a ~2 kyr average signal,  
169 which likely is more than the fire return interval at the time of deposition and thus represents an  
170 averaging of the overall fire signal through time and space. Therefore, the term 'fire activity' here  
171 describes the overall occurrences as increases and decreases in wildfires across the region.

172 In this study we measure the abundance of microcharcoal and macrocharcoal as a proxy for fire  
173 activity. The size of charcoal fragments is often used as an indicator if the fires were proximal or  
174 distal to the deposition site. Often larger more proximal charcoal particles are found in terrestrial  
175 biomes and their depositional environments, in soils, lakes and mires. In contrast, smaller charcoal  
176 particles that are wind-blown could potentially end up in a marine environment, as well as in more  
177 distal terrestrial settings. However, experimental research showed that riverine transport has the  
178 potential to carry the larger charcoal particles further away from shore, with the smaller charcoal  
179 particles becoming water saturated at a shorter distance and settling down closer to the shoreline  
180 (Nichols et al., 2000). In addition to this, other studies have indicated that larger charcoal particles (up  
181 to 7 cm) can be windblown and travel up to 50 km from the original source, depending mainly on  
182 their morphology (Woodward & Haines, 2020). Combined, charcoal size, shape, properties, wind  
183 direction, plume height, but also riverine and marine transportation, all have a different impact on the  
184 travel distance of different charcoal size classes. Hence, in the context of this study, no inferences can  
185 be made about the different size classes and therefore microcharcoal and macrocharcoal both serve as  
186 an overall indicator of fire activity.

187

#### 188 *Methods*

##### 189 Mass spectrometry $\delta^{13}\text{C}_{\text{org}}$ , TOC and $\text{CaCO}_3$

190 Bulk organic carbon-isotopes, TOC and carbonate content were measured to track changes in the  
191 carbon-cycle and changes in total organic matter in the studied interval. For the SPB interval (1271–  
192 1233 mbs) 50 samples and for the LPE (918–951 mbs) 193 samples were processed for carbon  
193 isotope mass spectrometry. Bulk rock samples were powdered using a pestle-a-mortar, weighed into  
194 centrifuge tubes, and decarbonated using 3.3 % HCl. Following, the samples were transferred to a hot  
195 bath (79 °C) for 1 h to remove siderite and dolomite. After this, the samples were centrifuged and the  
196 liquid decanted, this step repeated until the samples were neutralized (on average 2 times). Finally, the  
197 samples were oven-dried, re-powdered, and weighed (to measure  $\text{CaCO}_3$  loss) and transferred into  
198 small tin capsules for mass spectrometry (TOC and  $\delta^{13}\text{C}_{\text{org}}$ ), at the University of Exeter, Penryn  
199 Campus.

Formatted: Line spacing: 1.5 lines

Formatted: Font: Not Italic

Formatted: Font: (Default) Times New Roman, Font colour: Auto

Formatted: Font: (Default) Times New Roman, Font colour: Auto

200 Charcoal quantification and palynofacies

201 For the SPB interval, 54 samples were prepared for charcoal analysis and 42 for palynofacies at the  
202 University of Exeter, Streatam Campus. For the LPE interval, an additional 50 macrocharcoal  
203 samples were analysed, to compliment a total of 204 macrocharcoal samples for this interval. A total  
204 of 162 samples for palynofacies and 200 microcharcoal samples are included in the LPE study  
205 interval.

206 Rock samples of 10–30 g weight were split into 0.5 cm<sup>3</sup> fragments to minimize the breakage of the  
207 organic particles whilst optimizing the surface area for palynological acid maceration. First, the 190  
208 samples were treated with 10 % and 37 % HCl to remove carbonate. After this, hydrofluoric acid (40  
209 % HF) was added to remove silicates from the sample. The samples were left to digest for 48 h, after  
210 which cold concentrated HCl (37 %) was added to avoid calcium fluoride precipitation. Each sample  
211 was left to settle, after which it could be decanted and topped up with DI water, a step that was  
212 repeated ~6 times in order for the sample to neutralize.

213 After neutralizing, 5 droplets of the mixed residue were taken for the analysis of palynofacies (total  
214 particulate organic matter) prior to any sieving. The remaining residue was sieved through a 125 µm  
215 sieve and a 10 µm sieve to retrieve the macroscopic fraction (> 125 µm) and microscopic fraction  
216 (10–125 µm). Macroscopic charcoal (>125 µm) was quantified using a Zeiss Stemi microscope, with  
217 a 10 x 4 magnification lens and top lighting from a 'goose necked' light source. The entire  
218 macroscopic fraction was dispersed in a Petri dish filled with DI water and the number of charcoal  
219 particles counted and expressed per 10 g of processed rock (n/g). In some samples large clusters of  
220 matrix were not digested by the acid, in which case they were taken out and dry weighed to deduce  
221 the weight of the total processed rock. Charcoal particles are identified as opaque, black, angular,  
222 reflective of light, with lustrous shine, elongated, lacking brown edges, and splintering during  
223 breakage, and often showing the anatomical structure of the plant preserved (SI Fig. 1 and SI Table 2,  
224 Scott, 2000; Scott & Damblon, 2010).

225 Microscopic charcoal (10–125 µm) was analysed on a palynological slide. A known quantity of 125  
226 µl of the microscopic fraction was mounted onto microscopic slides using glycerine jelly. A  
227 transmitted light microscope (Olympus (BX53)) with a 40 x 10 magnification was used to count the  
228 charcoal particles. Four transects per slide were counted, one transect on the left, two in the middle,  
229 and one on the right of the coverslip. These data were then scaled up to the known quantity of the total  
230 sample (Belcher et al., 2005). Palynofacies were examined to record shifts in the type of organic  
231 matter (terrestrial vs marine) and potential changes in organic matter preservation and/or terrestrial  
232 runoff. Palynofacies were quantified using the optical light microscope and a minimum of 300 organic  
233 particles per palynological slide was counted. The types of organic matter were roughly grouped after  
234 Oboh-Ikuenobe et al. (2005): terrestrial palynomorphs (spores and pollen), marine palynomorphs

Deleted:



236 (dinoflagellates, acritarchs, prasinophytes and foraminifera test linings), fungal remains, structured  
237 phytoclasts (wood particles, parenchyma), unstructured phytoclasts (degraded plant remains),  
238 charcoal, black debris (palynomorphs filled with pyrite) and amorphous organic matter (AOM: fluffy,  
239 clotted and granular masses, colour ranging between almost colourless to yellow and pale brown).

#### 240 XRD clay mineralogy

241 A total of 55 samples were prepared for clay mineralogy spanning the SPB interval and 194 samples  
242 for the LPE interval. About 5 g of bulk-rock sample was gently crushed and powdered with an agate  
243 mortar, after which about 2–3 g of the powdered sample was decarbonated with a 0.2 M HCl solution.  
244 The samples were left to settle for 95 min, after which the suspended clay sized fraction (< 2 µm) was  
245 extracted with a syringe (following Stokes' law). The clay fraction was centrifuged and subsequently  
246 smeared and oriented on glass slides. The samples were analysed by X-ray diffraction (XRD) using a  
247 Bruker D4 Endeavour diffractometer (Bruker, Billerica, MA, USA) with Cu K $\alpha$  radiations, LynxEye  
248 detector and Ni filter under 40 kV voltage and 25 mA intensity at the Biogéosciences Laboratory,  
249 Université Bourgogne/FrancheComté, Dijon. Three runs were performed per sample to discriminate  
250 the clay phases: (1) air-drying at room temperature; (2) ethylene-glycol solvation for 24 h; (3) heating  
251 at 490 °C for 2 h, following Moore & Reynolds (1997). Comparing the three diffractograms obtained,  
252 the clay minerals were identified using their main diffraction (d0001) peak. The proportions of each  
253 clay mineral on glycolated diffractograms was estimated with the MACDIFF 4.2.5 software  
254 (Petschick, 2000). The identification of the clay minerals further follows the methods in Moore &  
255 Reynolds (1997) and Deconinck et al. (2019).

#### 256 Statistical analysis

##### 257 Orbital filters and the charcoal record

258 The Pliensbachian of the Mochras core has a well-established astrochronological framework (Ruhl et  
259 al., 2016; Hinnov et al., 2018; Storm et al., 2020; Hollaar et al., 2021; Pienkowski et al., 2021). Based  
260 on the existing cyclostratigraphy, the 100 kyr eccentricity cycle lies within the range of 3.2–10.2 m  
261 (Ruhl et al., 2016; Hinnov et al., 2018), 6.3–4.8 m (Storm et al., 2020), and ~5.3 m (Pieńkowski et al.,  
262 2021) for the here studied SPB and LPE intervals. These intervals each compromise ~7–8 short  
263 eccentricity cycles. No spectral analysis has been performed on the records presented here because of  
264 the limited time span represented. Instead, we compare the charcoal and clay records visually with the  
265 100 kyr and 405 kyr filters based on Ca and Ti (Ruhl et al., 2016; Hinnov et al., 2018). In SI Fig. 2 we  
266 overlay the 3.2 – 10 m filter (based on Ruhl et al., 2016) derived from the macrocharcoal record with  
267 the normalized dataset of the macrocharcoal record.

##### 268 Pearson correlation

269 A Pearson correlation was used to test for possible correlation between the charcoal abundance (both  
270 size fractions) and palynofacies and the significance using RMatlab2021b. The p value tests the

271 hypothesis of no correlation against the alternative hypothesis of a positive or negative correlation,  
272 with the significance level at  $\alpha=0.05$ . See SI Fig. 3.

273 Wilcoxon test

274 A Wilcoxon rank sum test was performed in RMatlab2023b to test the **null** hypothesis of equal means  
275 between the charcoal populations of the LPE and the SPB interval with the significance level at  $\alpha=$   
276 0.05. The test is performed for the macrocharcoal and microcharcoal records separately.

277 PCA analysis

278 Principal component analysis (PCA) was performed to explore the potential **covariance** of charcoal,  
279 clay mineralogy, palynofacies and mass-spectrometry records for the two studied intervals. This was  
280 executed in the software PAST (Hammer et al., 2001) on the normalized dataset (macrocharcoal,  
281 microcharcoal, TOC, CaCO<sub>3</sub>,  $\delta^{13}\text{C}_{\text{org}}$ , S/I, Sm/K, K/I, phytoclasts).

### 282 3 Results

283 The data presented here that cover the run-up to and onset of the SPB (1271–1233 mbs) show a ~1.8  
284 ‰ negative shift in  $\delta^{13}\text{C}_{\text{org}}$  spanning the end of the negative CIE limb in the Mochras borehole and  
285 reaching most negative values. The results of the LPE interval which encompass the run-up and onset  
286 of the LPE (951 – 918 mbs), show a rapid positive shift in the  $\delta^{13}\text{C}_{\text{org}}$  of ~1.8 ‰ (between 930.8 –  
287 930.4 mbs) (in agreement with Storm et al., 2020).

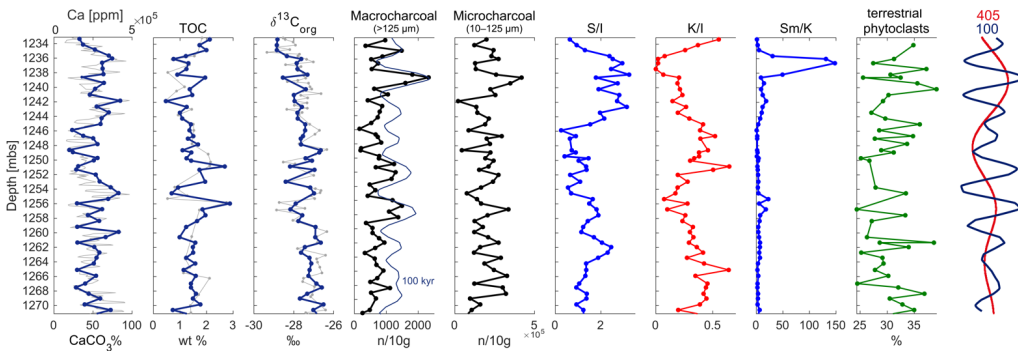
288 Large fluctuations are observed in the abundance of both macroscopic (>125  $\mu\text{m}$ ) and microscopic  
289 (10–125  $\mu\text{m}$ ) fossil charcoal for both CIEs. For the SPB, microcharcoal abundance fluctuates from  
290  $2 \times 10^4$ – $4.2 \times 10^5$  (mean  $2 \times 10^5$ ) particles per 10 g of sediment, and the number of macrocharcoal  
291 particles varies from 99–2327 (mean 787) particles per 10 g sediment (Fig. 2, SI Table 3). A similar  
292 trend is observed in both size fractions, with individual charcoal peaks fluctuating on a 2–4 m scale  
293 (Fig. 2). In the higher resolution LPE interval, metre-scale individual peaks of charcoal abundance are  
294 observed, with microcharcoal abundance fluctuating from  $4.5 \times 10^3$ – $4.3 \times 10^5$  (mean  $1.1 \times 10^5$ ) particles  
295 per 10 g of sediment, and the number of macrocharcoal particles varies from 8–2276 (mean 376)  
296 particles per 10 g sediment (Fig. 3, SI Table 3). Longer term fluctuations in the macrocharcoal record  
297 are also observed, with bundling of peaks visible every ~4–5 m. Micro- and macro-charcoal are more  
298 abundant in the SPB compared to the LPE (Fig. 4). The outcome of the Wilcoxon signed rank test  
299 confirms a different median of the SPB and LPE macrocharcoal (H0 rejected,  $p < 0.001$ ) and

Formatted: Font: (Default) Times New Roman, 11 pt, Font colour: Auto, Pattern: Clear

Formatted: Font: (Default) Times New Roman, 11 pt, Font colour: Auto, Pattern: Clear

300 microcharcoal (H0 rejected,  $p < 0.001$ ).

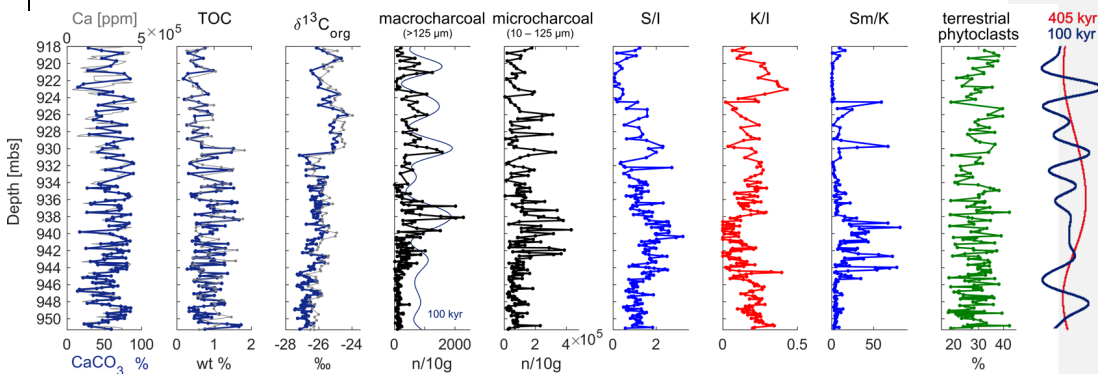
301



302 **Fig. 2: The SPB studied interval showing all proxies of this study in context of the orbital filters**  
 303 **(Ruhl et al., 2016).** The  $\text{CaCO}_3$ , TOC and  $\delta^{13}\text{C}_{\text{org}}$  (blue) data obtained for the present study are  
 304 plotted over previously published data (light grey – Ruhl et al., 2016; Storm et al., 2020). The  
 305 macrocharcoal abundance shows ~8 increases and decreases throughout the studied interval. These  
 306 high-low intervals in the macrocharcoal record correspond to the 100 kyr filter (blue; and see SI Fig.  
 307 2). The majority of macrocharcoal peaks are mirrored in the microcharcoal fraction. Alternating  
 308 phases of increase in the smectite/illite ratio (S/I) and the kaolinite/illite ratio (K/I) indicate swings in  
 309 the hydrological cycle. This is further indicated by the smectite/kaolinite ratio (Sm/K). The percentage  
 310 of terrestrial phytoclasts shows that the terrestrially sourced organic particles fluctuate around 30%  
 311 in the studied interval. Finally, the bandpass-filtered time series of the Ca-elemental XRF record of  
 312 Ruhl et al. (2016) indicate that the clay records shift dominance on a 405 kyr time scale. The peaks in  
 313 the macrocharcoal record occur on a 100 kyr time scale (see also SI Fig. 2).

Deleted:  
 Deleted: s  
 Deleted: based on the Ca-record

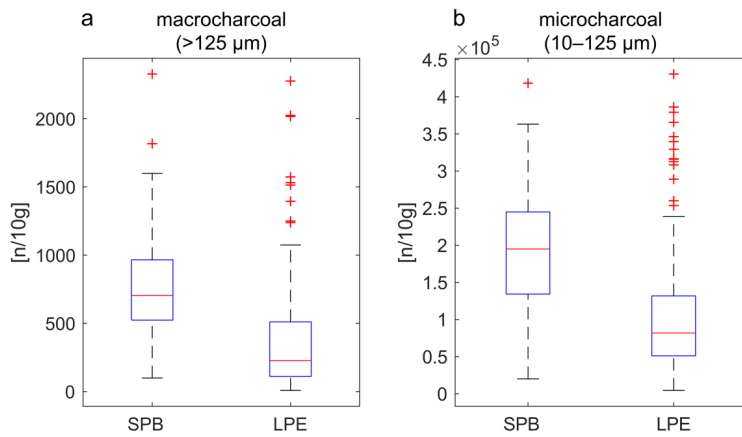
314



315 **Fig. 3: Synthesis of the LPE interval showing all proxies considered in this study in context of the**

319 *orbital filters (Ruhl et al., 2016). The CaCO<sub>3</sub>, TOC and δ<sup>13</sup>C<sub>org</sub> (blue) from Hollaar et al. (2023) are*  
320 *plotted over independently generated data (light grey - Ruhl et al., 2016; Storm et al., 2020). The*  
321 *macrocharcoal abundance shows ~7 peaks throughout the studied interval. These 7 increases and*  
322 *decreases in macrocharcoal abundance correspond to the 100 kyr eccentricity (in blue, see SI Fig. 2).*  
323 *The majority of macrocharcoal peaks are mirrored in the microcharcoal fraction. Alternating phases*  
324 *of increase in the smectite/illite ratio (S/I) and the kaolinite/illite ratio (K/I) indicate swings in the*  
325 *hydrological cycle. This is further indicated by the smectite/kaolinite ratio (Sm/K). The percentage of*  
326 *terrestrial phytoclasts shows that the terrestrially sourced organic particles fluctuate around 30 % in*  
327 *the studied interval. Finally, the orbital filters of Ruhl et al. (2016) are placed next to the proxy*  
328 *records. This shows that the clay records shift dominance on a 405 kyr time scale. The peaks in the*  
329 *macrocharcoal record occur on a 100 kyr time scale.*

330  
331 The palynofacies of both intervals is typically marine (AOM>58%). The proportion of terrestrial vs  
332 marine organic matter remains relatively stable through both the SPB and LPE, varying between 24.4  
333 and 39.1% (mean 30.7%), and 17.7 and 42.3% (mean 28.9%), respectively. Charcoal accounts for  
334 ~3.7% and ~4.5% of the total particulate organic matter, respectively for the SPB and the LPE  
335 intervals (SI Fig. 4). The abundance of macrocharcoal is not influenced by the percentage of terrestrial  
336 particulate organic matter through the SPB and LPE intervals (SPB  $r = -0.12$ ,  $p = 0.42$ ; LPE  $r = 0.06$ ,  
337  $p = 0.46$ ) and nor is the microcharcoal abundance for the SPB interval ( $r = 0.07$ ,  $p = 0.62$ ). However, a  
338 very weak correlation exists between the percentage of terrestrial phytoclasts and microcharcoal  
339 abundance in the LPE interval ( $r = 0.16$ ,  $p = 0.05$ ). These results suggest that the preservation and/or  
340 influx of terrestrial particulate organic matter is not the main driver of fluctuations in charcoal  
341 abundance.



342  
 343 **Fig. 4:** Distribution boxplots of the macrocharcoal and microcharcoal abundance of the SPB and  
 344 LPE studied intervals. (a) Average macrocharcoal abundance is higher in the SPB interval compared  
 345 to the LPE interval, however, the absolute minimum and maximum are similar. (b) Average  
 346 microcharcoal abundance is higher for the SPB compared to the LPE. The minimum number of  
 347 microcharcoal particles is lower for the LPE, however, the maximum microcharcoal abundance is  
 348 similar in both records.

349  
 350 The clay mineral assemblages of the SPB and LPE are dominated by illite, kaolinite and smectite (I-S  
 351 R0), with smectite increasing in parallel with decreases of illite and kaolinite (SI Fig. 5). Low  
 352 proportions of chlorite and sparse I-S R1 are present in the SPB record. Chlorite and I-S R1 are  
 353 generally low in the LPE record but increase between 924–219 mbs (SI Fig. 5). Two smectite-  
 354 enhanced phases occur for the SPB, at 1264–1255 mbs and 1245–1235 mbs. Both these phases are  
 355 coeval with high charcoal abundance (both size fractions) (Fig. 2, SI Fig. 6). Additionally, the LPE  
 356 interval encompasses two stratigraphic intervals rich in smectite; from 944–937 mbs and 931–924  
 357 mbs. Charcoal abundance (both size fractions) increases overall, and coevally with the S/I, over ~5 m  
 358 scale fluctuations, and decreases at levels with high K/I (Fig. 3, SI Fig. 7). The 3.2–10.2 m orbital  
 359 filter of the macrocharcoal records (interpreted as the 100 kyr eccentricity (Ruhl et al., 2016; Hinnov  
 360 et al., 2018; Storm et al., 2020; Pienkowski et al., 2021)), indicates that the observed fluctuations in  
 361 the macrocharcoal record occur with a 100 kyr periodicity (SI Fig. 2).

362  
 363 **4 Discussion**  
 364 *Charcoal transport and preservation*

Deleted:

366 The charcoal records for both the SPB and LPE intervals do not appear to be linked to the terrestrial  
367 influx of materials, as evidenced by the palynofacies. No ~~correlation or covariance exists between the~~  
368 abundance of terrestrial phytoclasts and the number of charcoal particles, which suggests that the  
369 abundance of charcoal is not a reflection of preservation and/or runoff changes. Inferred sea level  
370 changes during the LPE and the SPB could potentially have impacted the charcoal abundance record  
371 and the clay mineralogy. Transgression and relative sea-level rise during the SPB has been extensively  
372 recorded from the Boreal and Tethys regions, and from South America (e.g. Legarreta and Uliana,  
373 1996; de Graciansky et al., 1998; Hesselbo & Jenkyns, 1998; Danisch et al., 2019; Silva et al., 2021).  
374 The Late Pliensbachian is characterized by widespread regressive facies and inferred relative sea-level  
375 fall, likely indicating a closer proximity to shore also in the Mochras borehole. Fossil wood in the  
376 Mochras borehole has been shown to become more abundant at this time, suggesting a potential bias  
377 of higher terrestrial input from a nearby landmass (Ullmann et al., 2022). However, the mean  
378 abundance of macrocharcoal and microcharcoal is higher during the SPB (mean of 787 and  $2 \times 10^5$   
379 respectively) compared to the LPE (mean of 376 and  $1.1 \times 10^5$  respectively) in the Mochras borehole,  
380 suggesting that the shore proximity did not impact overall charcoal abundance. Similarly, the  
381 palynofacies analysis indicates that the mean abundance of terrestrial particulate organic matter during  
382 the SPB (30.7%) is not higher compared to the LPE (28.9%). Hence, we take this as strong evidence  
383 that the record of fossil charcoal records changes in wildfire activity.

Deleted: parallel trends are observed between

#### 384 *Orbital forcing of the hydrological cycle and fire*

385 Alternations in the dominance of smectite and kaolinite occur approximately every 10 m in both the  
386 LPE and SPB records. Kaolinite and smectite reflect hydrological changes in the palaeoenvironment  
387 of the Cardigan Bay Basin (Deconinck et al., 2019; Munier et al., 2021). As the smectite and kaolinite  
388 clay minerals are detrital in character and their abundance varies in opposition to one another (Fig. 2  
389 and 3), these clays are likely derived from pedogenic weathering profiles (Deconinck et al., 2019).  
390 Smectite preferentially forms under a ~~warm~~ and seasonally arid climate, similar to a monsoonal  
391 climate system or the winter-wet climate of the Mediterranean zone (Chamley, 1989; Deconinck et al.,  
392 2019). Kaolinite is indicative of an accelerated hydrological cycle ~~and an intensification of hydrolysis,~~  
393 increased runoff and a year-round wet climate (Chamley, 1989; Ruffell et al., 2002) either via  
394 formation in strong weathering profiles or via the physical erosion of kaolinite-bearing rocks  
395 (Chamley, 1989). ~~Pedogenic kaolinite preferentially forms in a hot climate (Chamley, 1989; Ruffell et~~  
396 ~~al., 2002).~~ At times of high smectite abundance, fire activity is greatest as observed from the macro-  
397 and micro-scopic charcoal fractions (Fig. 2 and 3). Based on the astrochronological framework of the  
398 Mochras borehole (Ruhl et al., 2016; Hinnov et al., 2018; Storm et al., 2020; Pieńkowski et al., 2021)  
399 these alternations appear to occur in concert with the 405 kyr long-eccentricity cycles (Fig. 2, Fig. 3).  
400 Eccentricity modulates the precession driven changes in seasonal and latitudinal distribution of  
401 insolation (Imbrie & Imbrie, 1980; Berger et al., 1989). One ~20 kyr precession cycle can represent a

Deleted: hot

404 strongly seasonal extreme climate for ~10 kyr and a weakly seasonal climate for the subsequent ~10  
405 kyr. The geological record averages the amplification or suppression of seasonality between years (SI  
406 Fig. 8). Eccentricity forcing modulates the amplitudes of these extremes in seasonality with  
407 periodicities of 100 kyr and 405 kyr.

408 In the Mesozoic, eccentricity maxima are commonly associated with dry climates that are disrupted  
409 by short and intense periods of precipitation and storm activity in the boreal landmasses bordering the  
410 NW Tethys (Martinez & Dera, 2015). In contrast, eccentricity minima are characterized by a more  
411 moderate seasonal contrasts and year-round wet conditions (Martinez & Dera, 2015). Eccentricity  
412 minima are linked to periods of enhanced runoff and weathering conditions as evidenced by high  
413 kaolinite content,  $^{87}\text{Sr}/^{86}\text{Sr}$ , and negative shifts in  $\delta^{18}\text{O}$  (Martinez & Dera, 2015). Therefore, we link  
414 the observed smectite-rich intervals to eccentricity maxima and the kaolinite-rich intervals to  
415 eccentricity minima. Charcoal abundance is highest during the seasonal climate of the eccentricity  
416 maxima for the SPB (Fig. 2 and 3), in agreement with the previous findings for the LPE (Hollaar et  
417 al., 2021, 2023).

418 Both the LPE and SPB study intervals span two 405-kyr cycles (Ruhl et al., 2016; Hinnov et al., 2018;  
419 Storm et al., 2020; Pieńkowski et al., 2021). The relative abundance of smectite and the abundance of  
420 charcoal both reach a peak during the maxima in the long eccentricity cycle, supporting the notion  
421 that orbitally driven changes in seasonal contrast in hydrolysis led to high fire activity. Within these  
422 long-term trends, the macrocharcoal record also shows ~5 m scale individual peaks or clusters in both  
423 the LPE and SPB records (SI Fig. 2, Fig. 2 and 3). Based on the existing age model (Ruhl et al., 2016;  
424 Hinnov et al., 2018; Storm et al., 2020; Pieńkowski et al., 2021) we derive that this is the expression  
425 of the ~100 kyr eccentricity cycle in the macrocharcoal record. The bandpass filtered time series  
426 representing the ~100 kyr cycle in the Pliensbachian of the Mochras core (derived from the Ca and  
427 macrocharcoal records), captures the observed ~5 m oscillations in the fire record (SI Fig. 2, Fig. 2  
428 and 3) (Ruhl et al., 2016; Hinnov et al., 2018; Storm et al., 2020; Pieńkowski et al., 2021).

429 The Sinemurian–Pliensbachian transition is generally associated with an overall warm and humid  
430 climate (Korte & Hesselbo, 2011; Gómez et al., 2016), and enhanced levels of runoff and weathering  
431 (Bougeault et al., 2017). The results presented here suggest that within this overall warm and humid  
432 background, orbital forcing created year-round wet periods, that were not conducive to frequent fire,  
433 alternating with periods that remained warm but had a more seasonal climate, that allowed ignition  
434 during the dry season. In contrast, the LPE, and the sediments of late Margaritatus ammonite  
435 chronozone formed in an overall semi-arid climate with proposed lower runoff levels from the land  
436 into the sea (Deconinck et al., 2019; Hollaar et al., 2021; 2023). During the run-up of the LPE we  
437 infer orbitally forced alternating climatic states of more extreme seasonality (high fire and smectite)  
438 and a more equitable year-round wet climate (low fire and high kaolinite) (Hollaar et al., 2021; 2023)

Deleted: ¶

Deleted:

Deleted:

Formatted: English (US)

442 acting within this overall semi-arid climate phase. Overall, kaolinite fluctuates in abundance in  
443 opposition to smectite, reflecting hydrological changes from wet and hot to semi-arid and hot, in  
444 agreement with high fire activity during a seasonal climate and fire suppression during a year-round  
445 wet climate for both the LPE and the SPB.

#### 446 *Vegetation, fire and the intermediate fire-productivity gradient*

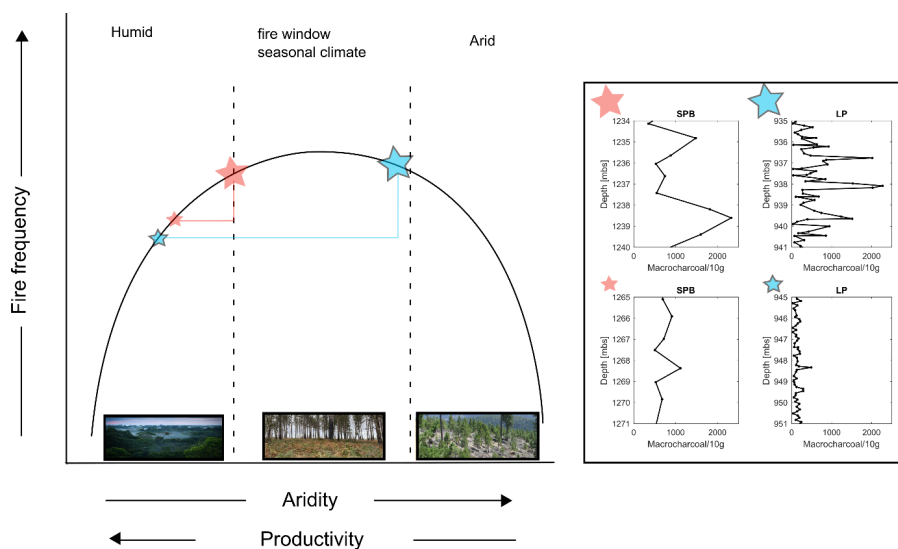
447 Fuel (vegetation biomass) and moisture status of the fuel, as governed by seasonal patterns in  
448 precipitation and temperature, are the core factors that influence fire behaviour and fire regime  
449 (Archibald et al., 2009; Cochrane & Ryan, 2009; Bradstock, 2010; Archibald et al., 2013; Bowman et  
450 al., 2014; Archibald et al., 2018). Ecosystems with limited wildfire activity are generally associated  
451 with either high precipitation and abundant primary productivity, or low productivity under strongly  
452 arid conditions (Pausas & Paula, 2012). In contrast, high wildfire activity occurs in climates that are in  
453 the middle of the productivity gradient, where during moist periods plant growth is rapid and biomass  
454 builds up forming a connected fuel structure. When followed by periods of drought the fuel moisture  
455 content is lowered enabling fire ignition and spread (Pausas & Paula, 2012). Additionally, higher  
456 sensitivity to fuel moisture levels in the tropical or mesic areas have been noted, where a small fall in  
457 fuel moisture content can lead to more flammable conditions (Cochrane, 2003). Such that the mid  
458 points in the intermediate fire-productivity gradient are further enhanced. The intermediate fire-  
459 productivity hypothesis (Pausas & Bradstock, 2007; Pausas & Ribeiro, 2013) conceptualizes this  
460 relationship between climate-vegetation-fire, where fire activity is plotted along an aridity and  
461 productivity gradient (Fig. 5). The observed alternating modes of high and low fire activity, as  
462 inferred from the lower Jurassic fossil charcoal record, during the onset of the SPB and LPE, likely  
463 indicates shifts in seasonality of the Cardigan Bay Basin hinterland and would place both the LPE and  
464 the SPB at intermediate productivity levels during maximum eccentricity forcing. The deep time  
465 combined fire and hydrological records we present here are in agreement with the intermediate  
466 productivity hypothesis of Pausas & Bradstock (2007) and indicate that even the very different plant  
467 functional types and different vegetation assemblages, e.g., a world without grasses, were still subject  
468 to this overall fire-productivity gradient control. We indicate on Fig. 5 how these ecosystems without  
469 grasses and other flowering plants may have looked in respect to typical Jurassic **fuel compositions**.  
470 We suggest that both the LPE and the SPB switched between a state of low fire (either limited by  
471 climatic aridity or the presence and presence and connectivity of fuel) and a state of high fire during  
472 which seasonal contrast is high and an ideal 'fire window' exists in which biomass built up during the  
473 wet season after which a fire-prone season followed (Fig. 5).

474

Deleted: d

Deleted: .





477

478 **Fig. 5: The LPE and SPB fire records placed on the intermediate productivity gradient.** The graph  
 479 is adapted from Pausas & Bradstock (2007). Fire frequency is highest in the middle of the hyperbola,  
 480 medium levels of aridity and productivity created a seasonal climate in which seasonal biomass  
 481 growth was possible (productivity) and seasonally the fuel moisture limits were lower in a season of  
 482 drought (aridity), this created the optimized 'fire window'. The SPB is plotted on this fire-productivity  
 483 gradient in red: the small star indicates the eccentricity minimum state and the large star the  
 484 eccentricity maximum state. The LPE is plotted on the fire-productivity gradient in blue, and again the  
 485 small star indicates the eccentricity minimum and the large star the eccentricity maximum. The LPE  
 486 has a larger range compared to the SPB, and experienced more fire suppression due to high humidity  
 487 levels during eccentricity minima, and also was closer to a productivity limitation state during the  
 488 eccentricity maximum.

Deleted: e

489 The studied Early Jurassic time-interval likely had five distinct biomes; a seasonal dry (summerwet or  
 490 subtropical) biome in the low latitudes, a desert biome in the subtropics, narrow latitudinal bands of a  
 491 winterwet biome at low-mid latitude, and warm temperate and cool temperate biomes at mid- and  
 492 high-latitudes, respectively (Rees et al., 2000; Willes and McElwain, 2014). The Cardigan Bay Basin  
 493 was likely positioned within the winterwet biome at approximately 35 °N (Torsvik et al., 2017). It  
 494 therefore would have sat within the bounds of the fire window of the intermediate fire-productivity  
 495 hypothesis (Fig. 5). The winterwet biome in both the Sinemurian and Pliensbachian stages were  
 496 dominated by conifers as the canopy tree, with a mid-canopy vegetation of cycads and tree-ferns, and  
 497 an understory mixture of seed ferns, horsetails and ferns that likely flourished during wetter periods  
 498 (Rees et al., 2000; Slater et al., 2019; Bos et al., 2023). This is evidenced from sporomorph data from

500 the Mochras borehole that hosts abundant fossil pollen in the Sinemurian and Pliensbachian (>94%)  
501 (Van de Schootbrugge et al., 2005). Additionally, nearby locations also show evidence of orbitally  
502 paced shifts in vegetation assemblages from sites at St. Audries Bay, UK and in NW Germany (Bonis  
503 et al., 2010; Bos et al., 2023).

504 During the 100 kyr eccentricity maxima in the UK pollen from the dry-adapted cheirolepidacean  
505 conifers is found to be highly abundant (Bonis et al., 2010). Whilst, in Germany a mire-conifer  
506 community is apparent with sporomorphs indicating variations in abundance of ferns and fern allies  
507 occurring over a 405-kyr eccentricity cycle, with ferns most abundant during eccentricity maxima  
508 (Bos et al., 2023).

509 Dry-adapted vegetation, such as the cheirolepidacean conifers likely thrived during more extreme  
510 seasonal droughts, maintaining their biomass. In contrast, ferns and fern allies, and mire-conifers as  
511 humid-loving plants would grow rapidly during sustained, year-round, periods of rainfall (eccentricity  
512 minima), likely inhabiting both open environments and colonising the understory of conifer forests.  
513 Furthermore, [these humid-loving plants](#) would also be able to build dense connected fuel loads during  
514 the wet-season of eccentricity maxima, that were then readily dried during the annual dry-season.  
515 Ferns, when cured, carry high intensity fires (Adie et al., 2011; Belcher and Hudspith, 2016) and  
516 during the Mesozoic ‘fern prairies’ have been linked to [intense](#) surface fires (Harris, 1981; Van  
517 Konijnenburg-Van Cittert, 2002; Collinson et al., 2007, 2009). Hence, they are suggested to have  
518 functioned in a similar fashion to support fires as grasslands and fern stands do today; Mesozoic fern  
519 prairies and savannahs therefore likely filled a similar ecological niche to grasses in the modern day  
520 (Belcher, 2013 and references therein). Ferns are indeed a common feature of Mesozoic charcoal  
521 assemblages, showing their association with fire throughout time (e.g. Collinson et al., 2000; Brown  
522 et al., 2012).

523 In the present-day, temperature is an important regulator of fire occurrence. Whilst dead fuel moisture  
524 (e.g. that of litter and cured herbaceous components) is primarily influenced by the variability in  
525 relative humidity, live fuels are controlled by the combination of temperature and moisture  
526 availability, where long periods of drought or heat wave extremes can strongly influence the  
527 flammability of live fuels. Sea surface temperatures during the Sinemurian and Pliensbachian were at  
528 times apparently higher than 28 °C (Robinson et al., 2017). But high-resolution temperature  
529 reconstructions are lacking for the Early Jurassic. Orbital forcing of regional–global seawater  
530 temperatures occurred throughout the Cenozoic (Westerhold et al., 2020), and likely also the  
531 Mesozoic; however, the climate response to changes in orbital insolation is non-linear, and the mean  
532 annual insolation is not impacted by precession (Rubicam, 1994). Therefore, the biomes of the SPB  
533 not only existed in an overall warm world that was characterized by background orbitally driven

534 climate shifts across the moister side of the fire-productivity gradient, but superimposed on this live  
535 fuels were also responsive to extreme weather linked to periods of drought and heat.

536

537 We propose that the overall humid climate of the SPB fits the high productivity scenario, in which the  
538 frequency of flammable conditions is the main factor controlling fire occurrences. No evidence was  
539 found to place the SPB on the productivity-limiting high-aridity side of the fire-productivity gradient,  
540 where fire frequency would have been mainly influenced by enhanced rainfall in an otherwise dry  
541 climate. These findings are in line with the presence of plant cuticle through the studied record,  
542 indicating the presence of vegetation throughout this time period and during both phases of high and  
543 low modes of fire activity. Hence, the SPB seems to conform to the humid and high productivity end  
544 of the aridity gradient (Fig. 5 red lines). Within these constraints (Fig. 5) the SPB is characterized by  
545 likely two states across the fire productivity gradient. The biome was situated at the wetter, low fire  
546 side of the fire-productivity gradient during eccentricity minima (Fig. 5), and at the seasonal, high fire  
547 end of the fire-productivity gradient during eccentricity maxima (but only for each precession half-  
548 cycle) (Fig. 5).

549 The fluctuations detected in the present study for the SPB occurred over both long-eccentricity and  
550 short eccentricity timescales in the macrocharcoal record, showing longer phases of overall  
551 enhancement of fire (405 kyr eccentricity) and relatively abrupt shifts from low to high fire and back  
552 again (~100 kyr eccentricity). For this reason, the SPB is placed on a steep portion of the fire-  
553 productivity gradient curve (Fig. 5). Overall, the mean charcoal abundance is relatively high, and no  
554 sustained periods of very low charcoal abundance are observed in the SPB record, which indicates  
555 that the climate never became too wet to fully limit fire activity at that time.

556 The Late Pliensbachian has been linked to a global cooling event, with a potential of 5–7 °C lowering  
557 in temperature inferred for the NW Tethys region (Korte et al., 2015). The atmospheric moisture  
558 holding capacity of a cooler climate is lower compared to a warm climate, in which a 1 °C cooling  
559 likely lowers the water holding capacity of air by 7% (Trenberth et al., 2005). The presence of  
560 terrestrial phytoclasts throughout confirms the presence of vegetation in the surrounding landmasses  
561 throughout this period. The mean abundance of charcoal for the LPE section is slightly lower than that  
562 of the SPB and the lowest charcoal abundances are coeval with a K/I enhancement, suggesting that  
563 during eccentricity minima environmental conditions moved further into the humid zone of the fire-  
564 productivity gradient (Fig. 5 blue line). Increasing eccentricity shifted the system to a more seasonal  
565 climate where the fire and clay records indicate the presence of a wet season that allowed for build-up  
566 of biomass followed by a dry season in which fire was able to be ignited and spread.

567 Conceptually, the relatively drier and cooler LPE climate would have resulted in conditions that are  
568 more arid, shifting to the biomass-limited part of the productivity/aridity – fire frequency gradient

Deleted:

Deleted: spectrum

Deleted:

572 during eccentricity maxima, compared to the SPB (Fig. 5 blue lines). This is supported by the large  
573 fluctuations observed between low fire frequency and high fire frequency for the LPE and the fact that  
574 estimated high fire periods did not occur suddenly, but rather were sustained over a larger part of the  
575 cycle. Therefore, the phase of highest fire frequency operating in the seasonal ‘fire window’ as  
576 indicated in figure 5 for the LPE (blue lines) likely occurred for a larger part of the fire productivity  
577 gradient. Hence, conditions across the LPE occurred across a wider range of the productivity/aridity  
578 and fire frequency gradients (Fig. 5 blue lines) compared to the SPB. There is no evidence that  
579 conditions ever became limited by aridity, and conditions during the LPE did not extend beyond the  
580 seasonal fire window into the arid part of the productivity/aridity gradient.

Deleted: spectrum of the

Deleted: spectrum of the fire frequency

581 Importantly, the Jurassic climate was overall warm and humid, about 5–10 °C warmer on global  
582 average compared to today (e.g., Rees et al., 2000; Sellwood & Valdes, 2008), with ~3.5–10 times the  
583 pre-industrial value of atmospheric  $p\text{CO}_2$  during the Early Jurassic (e.g. Retallack, 2001; Beerling &  
584 Royer, 2002; McElwain et al., 2005; Berner, 2006; Steinthorsdottir & Vajda, 2015; Li et al., 2020). In  
585 this context, it may not be surprising that a relative cooling event in the Early Jurassic did not lead to  
586 the aridity and biomass-limiting conditions observed during the last glacial period, at latitudes of ~38  
587 °C N (Daniau et al., 2007).

Deleted:

## 588 5 Conclusions

589 The study of two different climatic ‘background’ states, at the LPE and the SPB, shows that fire  
590 activity was strongly modulated by orbital eccentricity cycles. The 405 kyr shifts in the record of  
591 wildfire prevalence reflect similar changes also in the hydrological cycle (based on clay mineralogy  
592 data) showing that high fire activity occurred during periods of high seasonal contrast and that fire  
593 activity was suppressed during periods of high year-round humidity, because the latter would have  
594 enhanced the fuel moisture levels and prevented frequent ignition and sustained fire spread. The fire  
595 record of both climatic events is limited by the high fuel moisture levels during eccentricity minima,  
596 but fires were more prevalent during times of increased seasonality, every precession half-cycle  
597 during eccentricity maxima. Hence, during both events fire activity was limited by fuel moisture  
598 content and not by productivity. Both the SPB and the LPE climate systems were therefore situated on  
599 the moisture-limited side of the intermediate fire-productivity gradient (Fig. 5). Due to the lower  
600 moisture-holding capacity of cold air, the overall higher seasonality of the Late Pliensbachian and the  
601 more sustained high fire-frequency periods (based on the charcoal record for the LPE) we place the  
602 LPE towards the higher end of the aridity gradient, within maximum seasonality and maximum fire  
603 frequency window of the fire productivity graph (Fig. 5). The SPB fire regime reflected a more humid  
604 climate that shifted abruptly between low fire frequency to high fire frequency within less extreme  
605 bounds on the aridity gradient. This research reveals that the intermediate-fire productivity hypothesis  
606 (Pausas & Bradstock, 2007) can also be applied to high-resolution deep time records, before the  
607 evolution of grasses and that this hypothesis explains well the influence of orbital cycles within

611 different overall climate states, be they cooling or warming trends. The coupling of high-resolution  
612 clay mineralogy and fossil charcoal records, combined with constraints on orbital forcing at such  
613 time, allows for inferences on how Earth's natural climate state variability has driven shifts in  
614 terrestrial productivity through the geological past.

#### 615 **Acknowledgements**

616 This is a contribution to the JET project funded by the Natural Environment Research Council  
617 (NERC) (grant number NE/N018508/1). All authors acknowledge funding from the International  
618 Continental Scientific Drilling Program (ICDP) and TPH acknowledges funding from the University  
619 of Exeter.

#### 620 **Conflict of Interest**

621 The authors declare no conflicts of interest relevant to this study.

#### 622 **Data Availability Statement**

623 Supplementary data are available at the National Geoscience Data Centre at Keyworth (NGDC)  
624 at <https://doi.org/10.5285/1461dbe5-50a8-425c-8c49-ac1f04bcc271> (Hollaar, 2022) for the interval  
625 934–918 m. b.s. All data presented for the interval 951–934 m. b.s. are available at the National  
626 Geoscience Data Centre at Keyworth (NGDC) at [https://doi.org/10.5285/d6b7c567-49f0-44c7-a94c-  
627 e82fa17ff98e](https://doi.org/10.5285/d6b7c567-49f0-44c7-a94c-e82fa17ff98e) (Hollaar et al., 2021b). All data for the interval 1271–1233 mbs is deposited at the  
628 University of Exeter: <http://hdl.handle.net/10871/133255>.

#### 629 **Supporting Information**

630

#### 631 **References**

- 632 Adie, H., Richert, S., Kirkman, K. P., & Lawes, M. J. (2011). The heat is on: frequent high intensity  
633 fire in bracken (*Pteridium aquilinum*) drives mortality of the sprouting tree *Protea caffra* in temperate  
634 grasslands. *Plant Ecology*, 212, 2013 – 2022. <https://doi.org/10.1007/s11258-011-9945-8>
- 635 Archibald, S., Lehmann, C. E., Belcher, C. M., Bond, W. J., Bradstock, R. A., Daniou, A. L., et al.  
636 (2018). Biological and geophysical feedbacks with fire in the Earth system. *Environmental Research  
637 Letters*, 13(3), 033003. <https://doi.org/10.1088/1748-9326/aa9ead>
- 638 Archibald, S., Lehmann, C. E., Gómez-Dans, J. L., & Bradstock, R. A. (2013). Defining pyromes and  
639 global syndromes of fire regimes. *Proceedings of the National Academy of Sciences*, 110(16), 6442 –  
640 6447. <https://doi.org/10.1073/pnas.1211466110>

641 Archibald, S., Roy, D. P., van Wilgen, B. W., & Scholes, R. J. (2009). What limits fire? An  
642 examination of drivers of burnt area in Southern Africa. *Global Change Biology*, 15(3), 613 – 630.  
643 <https://doi.org/10.1111/j.1365-2486.2008.01754.x>

644 Beerling, D. J., & Royer, D. L. (2002). Fossil plants as indicators of the Phanerozoic global carbon  
645 cycle. *Annual Review of Earth and Planetary Sciences*, 30(1), 527 – 556.  
646 <https://doi.org/10.1146/annurev.earth.30.091201.141413>

647 Belcher, C. M., Collinson, M. E., & Scott, A. C. (2005). Constraints on the thermal energy released  
648 from the Chicxulub impactor: new evidence from multi-method charcoal analysis. *Journal of the  
649 Geological Society*, 162(4), 591 – 602. <https://doi.org/10.1144/0016-764904-104>

650 Belcher, C. M., Collinson, M. E., & Scott, A. C. (2013). A 450-Million-Year History of Fire. In C. M.  
651 Belcher (Eds.). *Fire Phenomena and the Earth System*. (pp. 240 – 241). London, UK: Wiley.

652 Belcher, C. M., & Hudspith, V. A. (2017). Changes to Cretaceous surface fire behaviour influenced  
653 the spread of the early angiosperms. *New Phytologist*, 213(3), 1521 – 1532.  
654 <https://doi.org/10.1111/nph.14264>

655 Berger, A., Loutre, M. F. & Dehant, V. Astronomical frequencies for pre-Quaternary palaeoclimate  
656 studies. *Terra Nova* 1, 474–479 (1989). <https://doi.org/10.1111/j.1365-3121.1989.tb00413.x>

657 Berner, R. A. (2006). GEOCARBSULF: a combined model for Phanerozoic atmospheric O<sub>2</sub> and  
658 CO<sub>2</sub>. *Geochimica et Cosmochimica Acta*, 70(23), 5653 – 5664.  
659 <https://doi.org/10.1016/j.gca.2005.11.032>

660 Bonis, N. R., Ruhl, M., & Kürschner, W. M. (2010). Milankovitch-scale palynological turnover across  
661 the Triassic–Jurassic transition at St. Audrie's Bay, SW UK. *Journal of the Geological Society*, 167(5),  
662 877 – 888. <https://doi.org/10.1144/0016-76492009-141>

663 Bos, R., Lindström, S., van Konijnenburg-van Cittert, H., Hilgen, F., Hollaar, T. P., Aalpoel, H. et al.  
664 (2023). Triassic-Jurassic vegetation response to carbon cycle perturbations and climate  
665 change. *Global and Planetary Change*, 228, 104211. <https://doi.org/10.1016/j.gloplacha.2023.104211>

666 Bougeault, C., Pellenard, P., Deconinck, J. F., Hesselbo, S. P., Dommergues, J. L., Bruneau, L., et al.  
667 (2017). Climatic and palaeoceanographic changes during the Pliensbachian (Early Jurassic) inferred  
668 from clay mineralogy and stable isotope (CO) geochemistry (NW Europe). *Global and Planetary  
669 Change*, 149, 139 – 152. <https://doi.org/10.1016/j.gloplacha.2017.01.005>

670 Bowman, D. M., Murphy, B. P., Williamson, G. J., & Cochrane, M. A. (2014). Pyrogeographic  
671 models, feedbacks and the future of global fire regimes. *Global Ecology and Biogeography*, 23(7),  
672 821 – 824. <https://doi.org/10.1111/geb.12180>

Field Code Changed

Field Code Changed

Formatted: English (UK)

Formatted: English (UK)

Formatted: English (UK)

673 Bradstock, R. A. (2010). A biogeographic model of fire regimes in Australia: current and future  
674 implications. *Global Ecology and Biogeography*, 19(2), 145 – 158. [https://doi.org/10.1111/j.1466-  
675 8238.2009.00512.x](https://doi.org/10.1111/j.1466-8238.2009.00512.x)

676 Brown, S. A., Scott, A. C., Glasspool, I. J., & Collinson, M. E. (2012). Cretaceous wildfires and their  
677 impact on the Earth system. *Cretaceous research*, 36, 162 – 190.  
678 <https://doi.org/10.1016/j.cretres.2012.02.008>

679 Chamley, H. (1989). *Clay Sedimentology*. Heidelberg: Springer Berlin Heidelberg.

680 Cochrane, M. A. (2003). Fire science for rainforests. *Nature*, 421(6926), 913 – 919.  
681 <https://doi.org/10.1038/nature01437>

682 Cochrane, M. A., & Ryan, K. C. (2009). Fire and fire ecology: Concepts and principles. *Tropical fire  
683 ecology*, 25 – 62. [https://doi.org/10.1007/978-3-540-77381-8\\_2](https://doi.org/10.1007/978-3-540-77381-8_2)

684 Collinson, M.E, Featherstone, C. Cripps, J.A, Nichols, G.J. & Scott, A.C. (2000). Charcoal-rich plant  
685 debris accumulations in the Lower Cretaceous of the Isle of Wight, England. *Acta Palaeobotanica*,  
686 Supplement 2, 93 – 105.

687 Collinson, M. E., Steart, D. C., Harrington, G. J., Hooker, J. J., Scob, A. C., Allen, L. O. et al. (2009).  
688 Palynological evidence of vegetation dynamics in response to palaeoenvironmental change across the  
689 onset of the Paleocene-Eocene Thermal Maximum at Cobham, Southern England. *Grana*, 48(1), 38 –  
690 66. <https://doi.org/10.1080/00173130802707980>

691 Collinson, M. E., Steart, D. C., Scob, A. C., Glasspool, I. J., & Hooker, J. J. (2007). Episodic fire,  
692 runoff and deposition at the Palaeocene–Eocene boundary. *Journal of the Geological Society*, 164(1),  
693 87 – 97. <https://doi.org/10.1144/0016-76492005-185>

694 Daniau, A. L., Bartlein, P. J., Harrison, S. P., Prentice, I. C., Brewer, S., Friedlingstein, P., et al.  
695 (2012). Predictability of biomass burning in response to climate changes. *Global Biogeochemical  
696 Cycles*, 26(4). <https://doi.org/10.1029/2011GB004249>

697 Daniau, A. L., Sánchez-Goñi, M. F., Beaufort, L., Laggoun-Défarge, F., Loutre, M. F., & Duprat, J.  
698 (2007). Dansgaard–Oeschger climatic variability revealed by fire emissions in southwestern  
699 Iberia. *Quaternary Science Reviews*, 26(9-10), 1369 – 1383.  
700 <https://doi.org/10.1016/j.quascirev.2007.02.005>

701 Danisch, J., Kabiri, L., Nutz, A., & Bodin, S. (2019). Chemostratigraphy of late Sinemurian–early  
702 Pliensbachian shallow-to deep-water deposits of the Central High Atlas Basin: Paleoenvironmental

Field Code Changed

703 implications. *Journal of African Earth Sciences*, 153, 239 – 249.

704 <https://doi.org/10.1016/j.jafrearsci.2019.03.003>

705 Deconinck, J. F., Hesselbo, S. P., & Pellenard, P. (2019). Climatic and sea-level control of Jurassic  
706 (Pliensbachian) clay mineral sedimentation in the Cardigan Bay Basin, Llanbedr (Mochras Farm)  
707 borehole, Wales. *Sedimentology*, 66(7), 2769 – 2783. <https://doi.org/10.1111/sed.12610>

Field Code Changed

708 De Graciansky, P. C., Dardeau, G., Dommergues, J. L., Durllet, C., Marchand, D., Dumont, T., et al.  
709 (1998). Ammonite biostratigraphic correlation and Early Jurassic sequence stratigraphy in France:  
710 comparisons with some UK sections. In: de Graciansky, P.C., Hardenbol, J., Jacquin, T., Farley, M. &  
711 Vail, P.R. (Eds.), Mesozoic and Cenozoic Sequence Stratigraphy of European Basins. *Special*  
712 *Publication of the Society for Sedimentary Geology (SEPM)*, 60, 583 – 622.

713 Glasspool, I. J., Edwards, D., & Axe, L. (2004). Charcoal in the Silurian as evidence for the earliest  
714 wildfire. *Geology*, 32(5), 381 – 383. <https://doi.org/10.1130/G20363.1>

715 Glasspool, I. J., & Gastaldo, R. A. (2022). Silurian wildfire proxies and atmospheric oxygen.

716 *Geology*. <https://doi.org/10.1130/G50193.1>

Field Code Changed

717 Gómez, J. J., Comas-Rengifo, M. J., & Goy, A. (2016). Palaeoclimatic oscillations in the  
718 Pliensbachian (Early Jurassic) of the Asturian Basin (Northern Spain). *Climate of the Past*, 12(5),  
719 1199 – 1214. <https://doi.org/10.5194/cp-12-1199-2016>

720 [Hammer, Ø., Harper, D. A. T., Ryan, P. D. 2001. PAST: Paleontological statistics software package  
721 for education and data analysis. \*Palaeontologia Electronica\*, 4\(1\): 9pp. \[http://palaeo-\]\(http://palaeo-<br/>722 electronica.org/2001\_1/past/issue1\_01.htm\)](http://palaeo-electronica.org/2001_1/past/issue1_01.htm)

Formatted: English (US)

Formatted: Font: Italic, Spanish

Formatted: Spanish

723 Harris, T. M. (1981). Burnt ferns from the English Wealden. *Proceedings of the Geologists'*  
724 *Association*, 92(1), 47 – 58. [https://doi.org/10.1016/S0016-7878\(81\)80019-3](https://doi.org/10.1016/S0016-7878(81)80019-3)

725 Haq, B. U. (2018). Jurassic sea-level variations: a reappraisal. *GSA today*, 28(1), 4 – 10.

726 <https://doi.org/10.1130/GSATG359A.1>

727 Hinnov, L. A., Ruhl, M. R., & Hesselbo, S. P. (2018). Reply to the Comment on “Astronomical  
728 constraints on the duration of the Early Jurassic Pliensbachian Stage and global climatic fluctuations”  
729 (Ruhl *et al.*, (2016). *Earth and Planetary Science Letters*, 455, 149 – 165).

730 <https://doi.org/10.1016/j.epsl.2017.10.061>

731 Hesselbo, S.P. & Jenkyns, H.C. (1998). British Lower Jurassic sequence stratigraphy. In: de  
732 Graciansky, P.C., Hardenbol, J., Jacquin, T., Farley, M. & Vail, P.R. (Eds.), Mesozoic–Cenozoic  
733 Sequence Stratigraphy of European Basins. *Special Publication of the Society for Sedimentary*  
734 *Geology (SEPM)*, 60, 561 – 581.

Formatted: German



735 Hollaar, T. P., Baker, S. J., Hesselbo, S. P., Deconinck, J. F., Mander, L., Ruhl, M., & Belcher, C. M.  
736 (2021). Wildfire activity enhanced during phases of maximum orbital eccentricity and precessional  
737 forcing in the Early Jurassic. *Communications Earth & Environment*, 2(1), 1 – 12.  
738 <https://doi.org/10.1038/s43247-021-00307-3>

739 Hollaar, T. P., Hesselbo, S. P., Deconinck, J. F., Damaschke, M., Ullmann, C. V., Jiang, M., &  
740 Belcher, C. M. (2023). Environmental changes during the onset of the Late Pliensbachian Event  
741 (Early Jurassic) in the Cardigan Bay Basin, Wales. *Climate of the Past*, 19(5), 979-997.  
742 <https://doi.org/10.5194/cp-19-979-2023>

743 Imbrie, J., & Imbrie, J. Z. (1980). Modeling the climatic response to orbital variations. *Science*,  
744 207(4434), 943 – 953. <https://doi.org/10.1126/science.207.4434.943>

745 Korte, C. & Hesselbo, S. P. (2011). Shallow marine carbon and oxygen isotope and elemental records  
746 indicate icehouse-greenhouse cycles during the Early Jurassic. *Paleoceanography*, 26(4).  
747 <https://doi.org/10.1029/2011PA002160>

748 Korte, C., Hesselbo, S. P., Ullmann, C. V., Dietl, G., Ruhl, M., Schweigert, G., & Thibault, N. (2015).  
749 Jurassic climate mode governed by ocean gateway. *Nature communications*, 6(1), 1 – 7.  
750 <https://doi.org/10.1038/ncomms10015>

751 Krawchuk, M. A., & Moritz, M. A. (2011). Constraints on global fire activity vary across a resource  
752 gradient. *Ecology*, 92(1), 121 – 132. <https://doi.org/10.1890/09-1843.1>

753 Legarreta, L., & Uliana, M. A. (1996). The Jurassic succession in west-central Argentina: stratal  
754 patterns, sequences and paleogeographic evolution. *Palaeogeography, Palaeoclimatology,*  
755 *Palaeoecology*, 120(3-4), 303 – 330. [https://doi.org/10.1016/0031-0182\(95\)00042-9](https://doi.org/10.1016/0031-0182(95)00042-9)

756 Li, X., Wang, J., Rasbury, T., Zhou, M., Wei, Z., & Zhang, C. (2020). Early Jurassic climate and  
757 atmospheric CO<sub>2</sub> concentration in the Sichuan paleobasin, southwestern China. *Climate of the Past*,  
758 16(6), 2055 – 2074. <https://doi.org/10.5194/cp-16-2055-2020>

759 Martinez, M. & Dera, G. (2015). Orbital pacing of carbon fluxes by a ~ 9-My eccentricity cycle  
760 during the Mesozoic. *Proceedings of the National Academy of Sciences*, 112, 12604 – 12609.  
761 <https://doi.org/10.1073/pnas.141994611>

762 McElwain, J. C., Wade-Murphy, J., & Hesselbo, S. P. (2005). Changes in carbon dioxide during an  
763 oceanic anoxic event linked to intrusion into Gondwana coals. *Nature*, 435(7041), 479 – 482.  
764 <https://doi.org/10.1038/nature03618>

Field Code Changed

Formatted: German

Formatted: German

Formatted: German

Field Code Changed

Formatted: German

- 765 Meyn, A., White, P. S., Buhk, C., & Jentsch, A. (2007). Environmental drivers of large, infrequent  
766 wildfires: the emerging conceptual model. *Progress in Physical Geography*, 31(3), 287 – 312.  
767 <https://doi.org/10.1177/0309133307079365>
- 768 Moore, D. M. & Reynolds Jr, R. C. (1997). *X-ray Diffraction and the Identification and Analysis of*  
769 *Clay Minerals*. Oxford: Oxford University Press.
- 770 Munier, T., Deconinck, J. F., Pellenard, P., Hesselbo, S. P., Riding, J. B., Ullmann, C. V., et al.  
771 (2021). Million-year-scale alternation of warm–humid and semi-arid periods as a mid-latitude climate  
772 mode in the Early Jurassic (late Sinemurian, Lurasian Seaway). *Climate of the Past*, 17(4), 1547 –  
773 1566. <https://doi.org/10.5194/cp-17-1547-2021>
- 774 Oboh-Ikuenobe, F. E., Obi, C. G. & Jaramillo, C. A. (2005). Lithofacies, palynofacies, and sequence  
775 stratigraphy of Palaeogene strata in Southeastern Nigeria. *Journal of African Earth Sciences*, 41, 79–  
776 101. <https://doi.org/10.1016/j.jafrearsci.2005.02.002>
- 777 Pausas, J. G., & Bradstock, R. A. (2007). Fire persistence traits of plants along a productivity and  
778 disturbance gradient in mediterranean shrublands of south-east Australia. *Global Ecology and*  
779 *Biogeography*, 16(3), 330 – 340. <https://doi.org/10.1111/j.1466-8238.2006.00283.x>
- 780 Pausas, J. G., & Paula, S. (2012). Fuel shapes the fire–climate relationship: evidence from  
781 Mediterranean ecosystems. *Global Ecology and Biogeography*, 21(11), 1074 – 1082.  
782 <https://doi.org/10.1111/j.1466-8238.2012.00769.x>
- 783 Pausas, J. G., & Ribeiro, E. (2013). The global fire–productivity relationship. *Global Ecology and*  
784 *Biogeography*, 22(6), 728 – 736. <https://doi.org/10.1111/geb.12043>
- 785 Petschick, R. MacDiff 4.1. 2. Powder diffraction software (2000). Available from the author at  
786 <http://www.geol.uni-erlangen.de/html/software/Macdiff.html>.
- 787 Pieńkowski, G., Uchman, A., Ninard, K., & Hesselbo, S. P. (2021). Ichnology, sedimentology, and  
788 orbital cycles in the hemipelagic Early Jurassic Lurasian Seaway (Pliensbachian, Cardigan Bay  
789 Basin, UK). *Global and Planetary Change*, 207, 103648.  
790 <https://doi.org/10.1016/j.gloplacha.2021.103648>
- 791 Rees, P. M., Ziegler, A. M. & Valdes, P. J. (2000). Jurassic phytogeography and climates: new data  
792 and model comparisons. In Huber, B. T., Macleod, K. G. & Wing, S. L. (Eds.), *Warm Climates in*  
793 *Earth History*. (pp. 297 – 318). Cambridge: Cambridge University Press.
- 794 Retallack, G. J. (2001). A 300-million-year record of atmospheric carbon dioxide from fossil plant  
795 cuticles. *Nature*, 411(6835), 287 – 290. <https://doi.org/10.1038/35077041>

Formatted: German

Formatted: German

Field Code Changed

796 Riding, J. B., Leng, M. J., Kender, S., Hesselbo, S. P., & Feist-Burkhardt, S. (2013). Isotopic and  
797 palynological evidence for a new Early Jurassic environmental perturbation. *Palaeogeography,*  
798 *Palaeoclimatology, Palaeoecology*, 374, 16 – 27. <https://doi.org/10.1016/j.palaeo.2012.10.019>

799 Robinson, S. A., Ruhl, M., Astley, D. L., Naafs, B. D. A., Farnsworth, A. J., Bown, P. R. et al. (2017).  
800 Early Jurassic North Atlantic sea-surface temperatures from TEX<sup>86</sup> palaeothermometry.  
801 *Sedimentology*, 64(1), 215 – 230. <https://doi.org/10.1111/sed.12321>

802 Rubincam, D. P. (1994). Insolation in terms of Earth's orbital parameters. *Theoretical and applied*  
803 *climatology*, 48, 195 – 202. <https://doi.org/10.1007/BF00867049>

804 Ruffell, A., McKinley, J. M. & Worden, R. H. (2002). Comparison of clay mineral stratigraphy to  
805 other proxy palaeoclimate indicators in the Mesozoic of NW Europe. *Philosophical Transactions of*  
806 *the Royal Society London A: Mathematical, Physical and Engineering Sciences*, 360, 675 – 693.  
807 <https://doi.org/10.1098/rsta.2001.0961>

808 Ruhl, M., Hesselbo, S. P., Hinnov, L., Jenkyns, H. C., Xu, W., Riding, J. B., et al. (2016).  
809 Astronomical constraints on the duration of the Early Jurassic Pliensbachian Stage and global climatic  
810 fluctuations. *Earth and Planetary Science Letters*, 455, 149 – 165.  
811 <https://doi.org/10.1016/j.epsl.2016.08.038>

812 Scott, A. C. (2000). The Pre-Quaternary history of fire. *Palaeogeography, Palaeoclimatology,*  
813 *Palaeoecology*, 164(1- 4), 281 – 329. [https://doi.org/10.1016/S0031-0182\(00\)00192-9](https://doi.org/10.1016/S0031-0182(00)00192-9)

814 Scott, A. C., & Damblon, F. (2010). Charcoal: Taphonomy and significance in geology, botany and  
815 archaeology. *Palaeogeography, Palaeoclimatology, Palaeoecology*, 291(1-2), 1 – 10.  
816 <https://doi.org/10.1016/j.palaeo.2010.03.044>

817 Sellwood, B. W., & Valdes, P. J. (2008). Jurassic climates. *Proceedings of the Geologists'*  
818 *Association*, 119(1), 5 – 17. [https://doi.org/10.1016/S0016-7878\(59\)80068-7](https://doi.org/10.1016/S0016-7878(59)80068-7)

819 Silva, R. L., Duarte, L. V., Wach, G. D., Ruhl, M., Sadki, D., Gómez, J. J. et al. (2021). An Early  
820 Jurassic (Sinemurian–Toarcian) stratigraphic framework for the occurrence of organic matter  
821 preservation intervals (OMPIs). *Earth-Science Reviews*, 221, 103780.

822 Slater, S. M., Twitchett, R. J., Danise, S., & Vajda, V. (2019). Substantial vegetation response to Early  
823 Jurassic global warming with impacts on oceanic anoxia. *Nature Geoscience*, 12(6), 462 – 467.  
824 <https://doi.org/10.1038/s41561-019-0349-z>

825 Steinthorsdóttir, M., & Vajda, V. (2015). Early Jurassic (late Pliensbachian) CO<sub>2</sub> concentrations  
826 based on stomatal analysis of fossil conifer leaves from eastern Australia. *Gondwana Research*, 27(3),  
827 932 – 939. <https://doi.org/10.1016/j.gr.2013.08.021>

Formatted: Dutch

Formatted: Dutch

Field Code Changed

Formatted: Spanish

Formatted: French

828 Storm, M. S., Hesselbo, S. P., Jenkyns, H. C., Ruhl, M., Ullmann, C. V., Xu, W., et al. (2020). Orbital  
829 pacing and secular evolution of the Early Jurassic carbon cycle. *Proceedings of the National Academy  
830 of Sciences*, 117(8), 3974 – 3982. <https://doi.org/10.1073/pnas.1912094117>

831 [The MathWorks Inc. \(2021\). MATLAB version: 9.11.0 \(R2021b\), Natick, Massachusetts: The  
832 MathWorks Inc. <https://www.mathworks.com>](#)

833 [The MathWorks Inc. \(2023\). MATLAB version: 9.14.0 \(R2023b\), Natick, Massachusetts: The  
834 MathWorks Inc. <https://www.mathworks.com>](#)

835 Torsvik, T. H., & Cocks, L. R. M. (2017). Jurassic. In *Earth History and Palaeogeography*.  
836 Cambridge: Cambridge University Press.

837 Trenberth, K. E., Fasullo, J., & Smith, L. (2005). Trends and variability in column-integrated  
838 atmospheric water vapor. *Climate dynamics*, 24(7), 741 – 758. [https://doi.org/10.1007/s00382-005-  
0017-4](https://doi.org/10.1007/s00382-005-<br/>839 0017-4)

Formatted: German

Field Code Changed

840 Ullmann, C. V., Szűcs, D., Jiang, M., Hudson, A. J., & Hesselbo, S. P. (2022). Geochemistry of  
841 microfossil, bulk rock and secondary calcite in the Early Jurassic strata of the Llanbedr (Mochras  
842 Farm) drill core, Cardigan Bay Basin, Wales, UK. *Journal of the Geological Society*, 179(1).  
843 <https://doi.org/10.1144/jgs2021-018>

844 van de Schootbrugge, B., Bailey, T. R., Rosenthal, Y., Katz, M. E., Wright, J. D., Miller, K. G., et al.  
845 (2005). Early Jurassic climate change and the radiation of organic-walled phytoplankton in the Tethys  
846 Ocean. *Paleobiology*, 31(1), 73 – 97. [https://doi.org/10.1666/0094-  
8373\(2005\)031<0073:EJCCAT>2.0.CO;2](https://doi.org/10.1666/0094-<br/>847 8373(2005)031<0073:EJCCAT>2.0.CO;2)

848 van der Werf, G. R., Randerson, J. T., Giglio, L., Collatz, G. J., Kasibhatla, P. S., & Arellano Jr, A. F.  
849 (2006). Interannual variability in global biomass burning emissions from 1997 to 2004. *Atmospheric  
850 Chemistry and Physics*, 6(11), 3423 – 3441. <https://doi.org/10.5194/acp-6-3423-2006>

851 Van Konijnenburg-Van Cibert, J. H. A. (2002). Ecology of some late Triassic to early Cretaceous  
852 ferns in Eurasia. *Review of Palaeobotany and Palynology*, 119(1-2), 113 – 124.  
853 [https://doi.org/10.1016/S0034-6667\(01\)00132-4](https://doi.org/10.1016/S0034-6667(01)00132-4)

854 Westerhold, T., Marwan, N., Drury, A. J., Liebrand, D., Agnini, C., Anagnostou, E. et al. (2020). An  
855 astronomically dated record of Earth's climate and its predictability over the last 66 million years.  
856 *Science*, 369(6509), 1383 – 1387. <https://doi.org/10.1126/science.aba6853>

857 Willes, K. & McElwain, J. (2014) *The Evolution of Plants*, Oxford University Press.